Exp Fluids (2012) 52:1593–1609
DOI 10.1007/s00348-012-1274-8

RESEARCH ARTICLE

Wingtip vortex control via the use of a reverse half-delta wing

T. Lee · Y. Y. Su

Received: 1 October 2011 / Revised: 26 January 2012 / Accepted: 30 January 2012 / Published online: 19 February 2012

Abstract The effect of a 65° sweep reverse half-delta wing (RHDW), mounted at the squared tip of a rectangular NACA 0012 wing, on the tip vortex was investigated experimentally at $Re = 2.45 \times 10^5$. The RHDW was found to produce a weaker tip vortex with a lower vorticity level and, more importantly, a reduced lift-induced drag compared to the baseline wing. In addition to the lift increment, the RHDW also produced a large separated wake flow and subsequently an increased profile drag. The reduction in lift-induced drag, however, outperformed the increase in profile drag and resulted in a virtually unchanged total drag in comparison with the baseline wing. Physical mechanisms responsible for the RHDW-induced appealing aerodynamics and vortex flow modifications were discussed.

List of symbols

AR	Aspect ratio $= b^2/S_{\text{total}}$
b	Wing span $= 2s$
b'	Effective span
c	Chord
c_{RHDW}	RHDW root chord
C_D	Total drag coefficient $= C_{D_i} + C_{D_p}$
C_{D_i}	Lift-induced drag coefficient $= D_i/\frac{1}{2}\rho_\infty u_\infty^2 S_{\text{total}}$
C_{D_p}	Profile drag coefficient
C_L	Total lift coefficient
D_i	Lift-induced drag
e	Span efficiency factor
r	Radial distance
r_c	Vortex core radius
Re	Chord Reynolds number $= u_\infty c/\upsilon$
s	Semi-span
s_{RHDW}	RHDW semi-span
S_{BW}	Baseline-wing area
S_{RHDW}	RHDW surface area
S_{total}	Total wing area $= S_{\text{BW}} + S_{\text{RHDW}}$
u_c	Axial core velocity
u_∞	Freestream velocity
u, v, w	Mean axial, vertical and spanwise velocity
v_θ	Tangential velocity
x, y, z	Streamwise, vertical and spanwise direction
α	Angle of attack
α_{ss}	Static-stall angle
Λ	Sweep angle
ζ	Streamwise vorticity
Γ	Vortex circulation
Γ_c	Core circulation
Γ_o	Total circulation
ρ_∞	Freestream fluid density
ψ	Stream function
ϕ	Velocity potential
υ	Fluid kinematic viscosity

T. Lee (✉) · Y. Y. Su
Department of Mechanical Engineering, McGill University, Montreal, QC H3A 2K6, Canada
e-mail: tim.lee@mcgill.ca

1 Introduction

It is known that delta wings have desirable low compressibility drag at high speeds and good high angle of attack characteristics at low speeds. The aerodynamic characteristics and the flow phenomena associated with the leading-edge vortices, including its breakdown, developed on both non-slender and slender delta wings have been investigated extensively by researchers elsewhere. Excellent reviews of delta wings are given by Nelson and

Pelletier (2003), Gursul et al. (2005), and Breitsamter (2008). Recently, Altaf et al. (2011) investigated the trailing vortex wake behind a reverse 75° sweep delta wing, with a windward bevel angle of 20°, by using particle image velocimetry (PIV) at a chord Reynolds number $Re = 3.82 \times 10^5$ at $x/c = 0.359$ and 2.418 (downstream from the trailing apex point) for various angles of attack and roll angles. CFD simulations of the streamlines, velocity vectors, and surface pressure contours over the reverse delta wing were also obtained to supplement the PIV measurements. Meanwhile, the aerodynamic load coefficients of the reverse delta wing were also acquired and were compared with a conventional delta wing of the same sweep angle. They showed that the peak tangential velocities of the reverse delta wing had a trend similar to that of a delta wing for $\alpha > 5°$ and that at a particular angle of attack the reverse delta wing-generated tip vortex exhibited a lower magnitude of tangential velocity, circulation, and vorticity than a delta wing vortex. The flow characteristics along the upper surface of the reverse delta wing were, however, not reported. Altaf et al. (2011) further noticed that the reverse delta wing was found to lie outside each tip vortices zone of influence. In contrast, the vortices over a delta wing were entirely over the wing, rendering a higher lift than a reverse delta wing. The lowered drag generated by the reverse delta wing, however, overcame the loss in lift and produced an improved lift-to-drag ratio compared to the delta wing. It is noteworthy that Norris (1998) had also shown that the reverse delta wing design can create additional lift at low speeds, reducing power requirements and therefore noise during the environmentally crucial takeoff and landing phases. Elsayed et al. (2008) further suggested that a reverse delta wing can be used as a wake alleviation add-on device, which modifies the vortex roll-up process and leads to a rapid diffusion of vorticity and, subsequently, an enhanced wake-vortex decay.

Note that, in addition to the continuous effort made by researchers elsewhere to enhance the wing lift generation capability, the alleviation of the ensuing two energetic counter-rotating streamwise vortices (generated behind the lifting wings) continues to pose a challenge to aerodynamicists and the aviation industry. These wingtip vortices not only impose wake-vortex hazard, which decreases airport capacity, but also produces lift-induced drag, which degrades the wing aerodynamic performance. Robinson (1996) estimated that the current FAA wake-turbulence separations result in a 12% loss in airport capacity when arrivals comprise 50% of the operations. Moreover, the recent winglet retrofit order of Southwest Airline for 169 Boeing 737-700/800, capable of saving 92,000 gallons of fuel per year per aircraft (AW&ST 2003), further reinforces the paramount importance of the wingtip vortices and their control. Extensive investigations have been carried out by researchers elsewhere to investigate the tip vortex structure and its dissipation or persistence in both intermediate and far wakes. An in-depth review of the archived wake-vortex studies in the intermediate and far fields behind the wing tips is given by Spalart (1998) and Rossow (1999). In addition, it is also known that the near-field tip vortex flow characteristics play an important role in the understanding and control of wingtip vortex. A number of experiments (for example, Corsiglia et al. 1973; Francis and Kennedy 1979; Green and Acosta 1991; McAlister and Takahashi 1991; Shekarriz et al. 1993; Chow et al. 1997; Ramaprian and Zheng 1997; Birch and Lee 2004; Lee and Pereira 2010) have been conducted to characterize the dynamics of the initial rollup of a tip vortex around the wing tip and its subsequent development in the near field (normally within two or three chord lengths downstream of the wing trailing edge) of a wing. Meanwhile, various passive control devices such as winglets, spoilers, stub/subwing, and porous tips and leading edges (Spillman 1978; Tangler 1978; Muller 1990; Naik and Ostowari 1990; Lee 1994; Liu et al. 2001; Lee and Lee 2006) have also been attempted to modify the strength and structure, including the trajectory, of a tip vortex.

The objective of this study was to explore the potential reduction of the wingtip vortex strength and the subsequent lift-induced drag by the use of a 65° sweep reverse half-delta wing (RHDW), mounted at the squared tip of a rectangular NACA 0012 wing, at $Re = 2.45 \times 10^5$ in a subsonic wind tunnel by using a miniature seven-hole pressure probe. The lift-induced drag was computed, based on the vorticity inferred from the measured cross-flow velocity field, by using the Maskell induced drag model (1973). Special attention was also given to the impact of the addition of the RHDW on the variation of the axial velocity and vorticity flowfields both along the wing tip and in the near field behind the RHDW wing configuration. Force-balance measurements and smoke-wire flow visualizations were also obtained to supplement the flowfield measurements. Physical mechanisms responsible for the observed modifications in the aerodynamic performance and vortical flow structures were also discussed.

2 Experimental methods

The experiment was conducted in the $0.9 \times 1.2 \times 2.7$ m^3 low-turbulence, suction-type subsonic wind tunnel at McGill University. A CNC-machined square-tipped, aluminum rectangular NACA 0012 wing, with a chord $c = 28$ cm and a semi-span $s = ½b = 50.8$ cm, was used as the main wing. The wing model was mounted vertically at the center of the wind tunnel test section. A 2-mm-thick

circular endplate, of 50 cm diameter, with a sharp leading edge was fitted to one end, located 10 cm from the floor of the test section, of the wing model to mitigate the free end effects and its interaction with the wind-tunnel wall boundary-layer flow. The origin of the co-ordinate system was located at the leading edge of the wing. The wing pitch axis was located at ¼-c location. Boundary-layer transition was fixed on the upper and the lower wing surfaces by using a trip strip (of a width of 5%c) located at 10%c downstream of the wing leading edge. The tip of the semi-wing model was also equipped with a RHDW, with $\Lambda = 65°$, $c_{\mathrm{RHDW}} = 28$ cm, $s_{\mathrm{RHDW}} = 13.6$ cm and an area S_{RHDW} of 190.4 cm^2, which gave a 13.4 and 41.8% increase in the total semi-wing area S_{total} ($=S_{\mathrm{BW}} + S_{\mathrm{RHDW}}$) and AR compared to the baseline wing. The schematics and dimensions of the wing model and the RHDW are given in Fig. 1a. The RHDW, pitchable at ½c location, was made of aluminum plate with a thickness of $t = 3.2$ mm (or $t/c = 1.1\%$), and a windward bevel of 15°. The RHDW deflection was fixed at zero, and the chord Reynolds number was fixed at 2.45×10^5.

The three components of the mean vortex flowfield (u, v, w), behind the NACA 0012 wing with and without the RHDW, were measured first in plane perpendicular to the freestream velocity at $x/c = 3$ for $\alpha = 2°$ to 18°, with an increment of 2°, by using a miniature seven-hole pressure probe. The vortical flow structures developed both along the tip of the baseline wing and the RHDW-equipped wing (for $x/c < 1.0$) and in the near field (for $1 < x/c \leq 4$) were also acquired at $\alpha = 10°$. The seven-hole pressure probe, of a diameter of 2.6 mm, was calibrated in situ before the installation of the model. Eight Honeywell model DC002NDR5 pressure transducers (seven for the probe and one for tunnel reference total pressure) were used to maximize the data rate of the probe measurement system at each measurement location. The pressure signals were sampled at 500 Hz with a sampling time of 5 s and were recorded on a PC through a 16-bit A/D converter board. Probe traversing was achieved through a custom-built computer-controlled traversing system. Each data plane taken in the near field of the wing models, covering up to 75%s, had 2,400 measuring grid points with an increment of $\Delta y = \Delta z = 3.2$ mm (or 1.15%c), except along the span of the wing where $\Delta z = 6.4$ mm. A finer grid size of 0.6%c was also used to determine the core vortex flow characteristics. Figure 1b shows the adaptive grid method

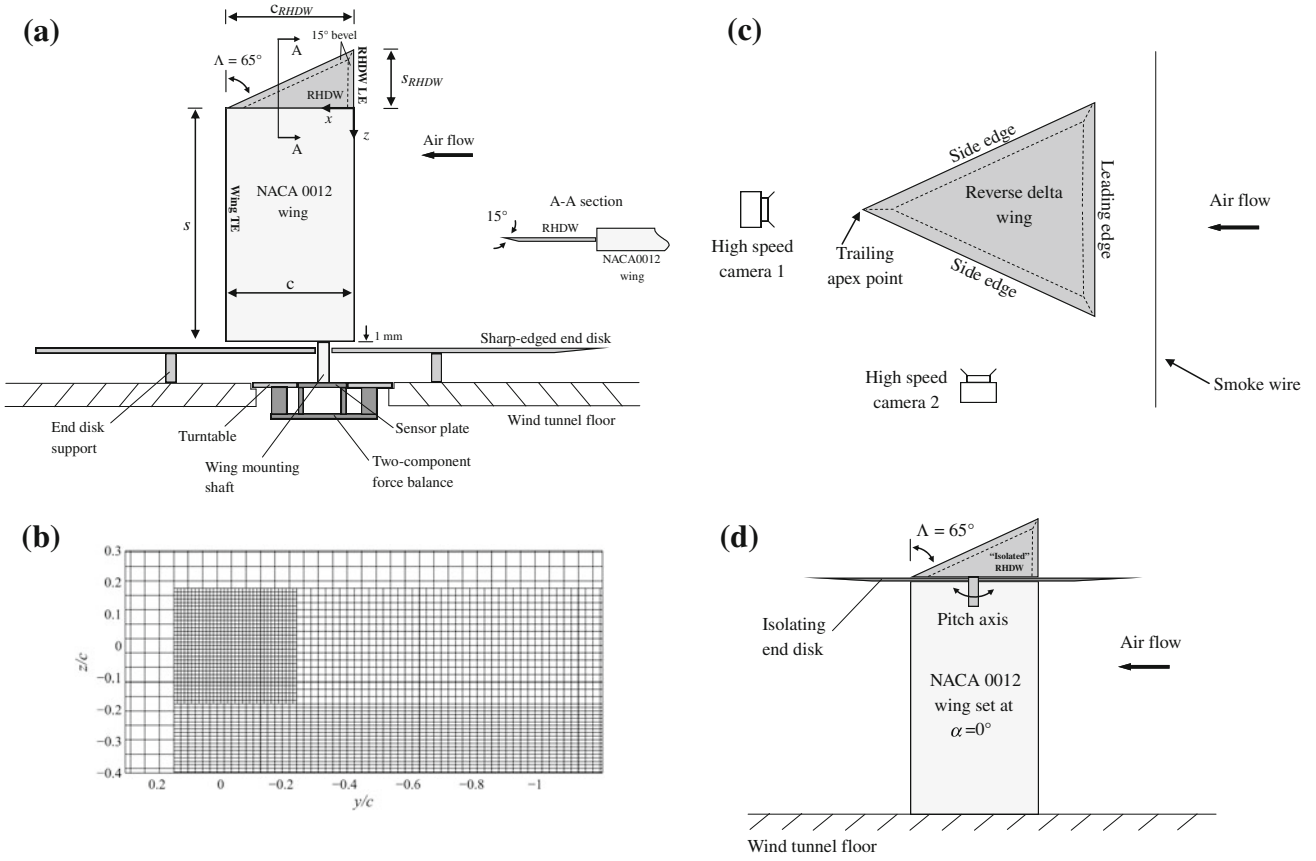

Fig. 1 Schematics of experimental setup. **a** RHDW wing model and force balance, **b** adaptive grid method employed in wake scan, **c** smoke-wire flow visualization, and **d** "isolated" reverse half-delta wing

employed in the present near-field wake measurements. The lift-induced drag was computed, based on the vorticity distributions inferred from the measured vw-cross-flow fields, via the Maskell model. The maximum uncertainty for the experimental data is as follows (Birch and Lee 2004): mean velocity 3.5%, vorticity component 8%, and vortex radius 4%.

For lift and drag measurements, the finite wing model was mounted vertically on an external two-component force balance located below the wind tunnel (see also Fig. 1a). The wing model was mounted vertically above a 0.45 × 60 × 60 cm aluminum endplate with sharp leading edges, fixed to the bottom wall of the test section, and an aerodynamic fairing was placed around the shaft to isolate it from the tunnel flow. The gap between the wing model and the endplate was kept at less than 1 mm or 0.1%s (or <0.05%b as suggested by Barlow et al. (1999)) to minimize leakage of flow through the gaps. The maximum uncertainty for the lift C_L and drag coefficients C_D is ±0.05 and ±0.009, respectively.

Smoke-wire flow visualization was also conducted by using a nichrome wire with a diameter of 105 μm for both the reverse full delta wing and RHDW-equipped wing at $Re = 3 \times 10^4$. Both the end view and side view of the vortical flow patterns were recorded simultaneously by using two high-speed digital cameras (Casio model EX-FH25) at 120 frames per second. Figure 1c shows the schematic of the arrangement of the smoke wire and cameras.

3 Results and discussion

Before the discussion of the impact of the addition of the 65° sweep RHDW, to the squared tip of the rectangular NACA 0112 wing, on the tip vortex and the accompanied lift-induced drag, the smoke-wire flow patterns of the 65° sweep reverse full delta wing, positioned at 10° and 25°, were illustrated first in Fig. 2a–f. The flow is from right to left. The smoke wire was positioned about 12 mm upstream and 3 mm beneath the leading edge of the reverse delta wing. The formation and growth of the two counter-rotating streamwise vortices, generated by the rollup of the upper and lower wall-shear layers (along the leading edge of the reverse delta wing), as they progressed downstream can be clearly seen in Fig. 2a, b, d, e. The origin and presence of these vortices can be better explained from Fig. 10 of Altaf et al. (2011). The spanwise leading vortex filament was not visualized in the present experiment, due to the relative position of the smoke wire to the leading edge of the reverse delta wing. Nevertheless, these vortices were also found to lie outside and above the reverse full delta wing (see Fig. 2a, b, d, e). That is, the reverse full delta wing was found to lie outside each tip vortice's zone of influence, a phenomenon similar to the CFD simulations of Altaf et al. (2011). These vortices also became more diffused and less discernible as α was increased, for example, from $\alpha = 10°$ to 25° (e.g., see Fig. 2d–f).

3.1 Vortex flow characteristics at $x/c = 3$

Figure 3a–e illustrate the impact of the RHDW on the normalized iso-vorticity contours of the tip vortex generated behind the RHDW-equipped wing at $x/c = 3$ for different angles of attack. The baseline-wing results are also included in Fig. 3f–h to serve as a comparison. Note that for clarity, only the iso-$\zeta c/u_\infty$ contours of the tip vortex flow region are presented here. The dotted and dashed lines denote the leading edge of the RHDW and the wing trailing edge, respectively. The streamwise vorticity ζ ($=\partial w/\partial y - \partial v/\partial z$) was calculated from the measured mean cross-flow (vw) velocity components by using a central differencing scheme to evaluate the derivatives. The addition of the RHDW led to a weaker tip vortex of a lowered vorticity level, including its peak value ζ_{peak} (see also Fig. 4a), compared to the baseline wing at the same α. The variation of normalized vortex core flow parameters, such as ζ_{peak}, core circulation Γ_c, core radius r_c, and the peak tangential velocity $v_{\theta,peak}$ with α, is summarized in Fig. 4a–d, respectively. The core circulation was calculated by summing the vorticity multiplied with the incremental area of the measuring grid. The core radius was obtained from the vortex flow distribution across the vortex center presented in Fig. 5a and is defined as the radius at which the tangential velocity v_θ is a maximum. The vortex center was located by the position of the maximum vorticity ζ_{peak} (Fig. 5b). Figure 4b–d further show that the tip vortex of the RHDW configuration also had a significantly lowered core circulation with a smaller core radius (up to $\alpha \leq 12°$) and $v_{\theta,peak}$ compared to the baseline wing, as a result of the unique vortex formation process of the reverse delta wing (as discussed in Fig. 2a, b, d, e) in opposition to the shear-layer rolling-up process oftentimes observed along the squared tip of the rectangular NACA 0012 wing (as shown, for example, in Fig. 5 of Lee and Pereira 2010). A 43, 56.4, 25.3 and 42% reduction in ζ_{peak}, Γ_c, r_c, and $v_{\theta,peak}$, for instance, at $\alpha = 10°$, respectively, was obtained compared to the baseline wing. The values of Γ_c, r_c, and $v_{\theta,peak}$ were also found to increase monotonically with increasing α (for $\alpha < \alpha_{ss}$) for both baseline wing and RHDW wing tested in the present study. The increase of the core radius with α can be attributed to the thickening of the shear layer thickness, as α was increased, that rolled up into the vortex. Meanwhile, the subsequent increase in Γ_c and $v_{\theta,peak}$ can be attributed to the increase in lift as α was increased.

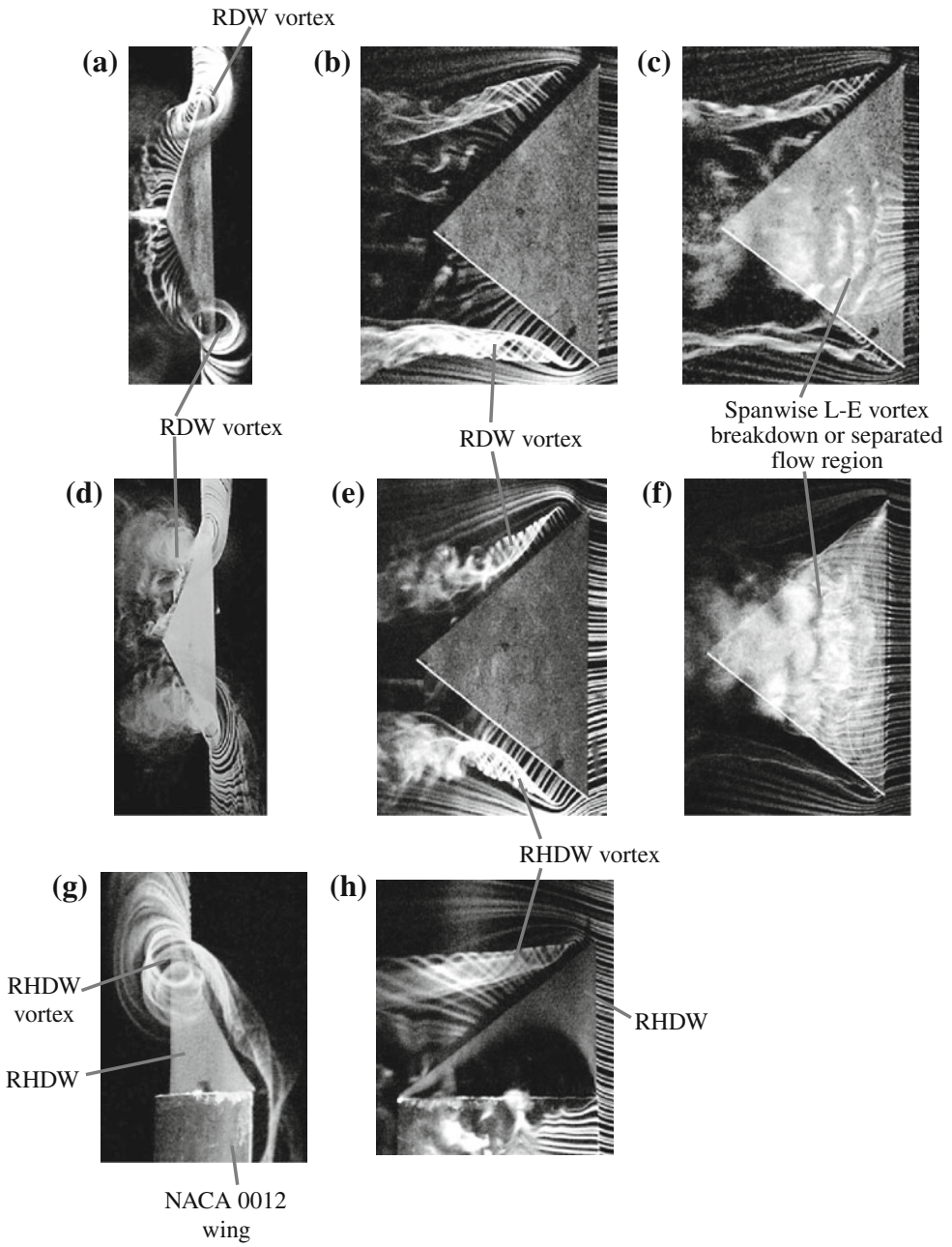

Fig. 2 Photographs of smoke-wire visualized flow patterns at $\alpha = 10°$. RDW at $\alpha = 10°$: **a** end view and **b**, **c** side views. RDW at $\alpha = 25°$: **d** end view and **e**, **f** side views. RHDW-equipped wing: **g** end view and **h** side view. Flow is from *right* to *left*. RDW and RHDW denote reverse (full) delta wing and reversed half-delta wing, respectively

It is of interest to note that, regardless of the presence of the RHDW and α, the vorticity distribution of the inner-flow region of the tip vortex (characterized by $v_{\theta,\max} \approx |v_{\theta,\max}|$) also attained near axisymmetry at $x/c = 3$. The nearly axisymmetric inner-flow behavior can be demonstrated from the radial circulation $\Gamma(r)$ distribution of the tip vortex presented in Fig. 5c. For both baseline wing and RHDW-equipped wing, the near-field tip vortex at $x/c = 3$ was found to follow the $\Gamma(r) \sim r^2$ profile for $r/r_c < 0.4$ and vary logarithmically for $0.5 < r/r_c < 1.4$, regardless of α [as observed by Ramaprian and Zheng (1997) and Birch and Lee (2004)]. Note that even though the vortex sheets roll up quickly and asymptotically in the near wake, it generally takes many wing spans behind the aircraft before the fully rolled-up condition and a state of equilibrium is reached. The empirical curve-fit relationships that describe the inner-core region and the region where the $\Gamma(r)$ distribution is logarithmic, according to Hoffmann and Joubert (1963) and Phillips (1981), are $\Gamma(r)/\Gamma_c = a_1(r/r_c)^2$ for $r/r_c < 0.4$ and $\Gamma(r)/\Gamma_c = a_2\log(r/r_c) + a_3$ for $0.5 < r/r_c < 1.4$. The curve-

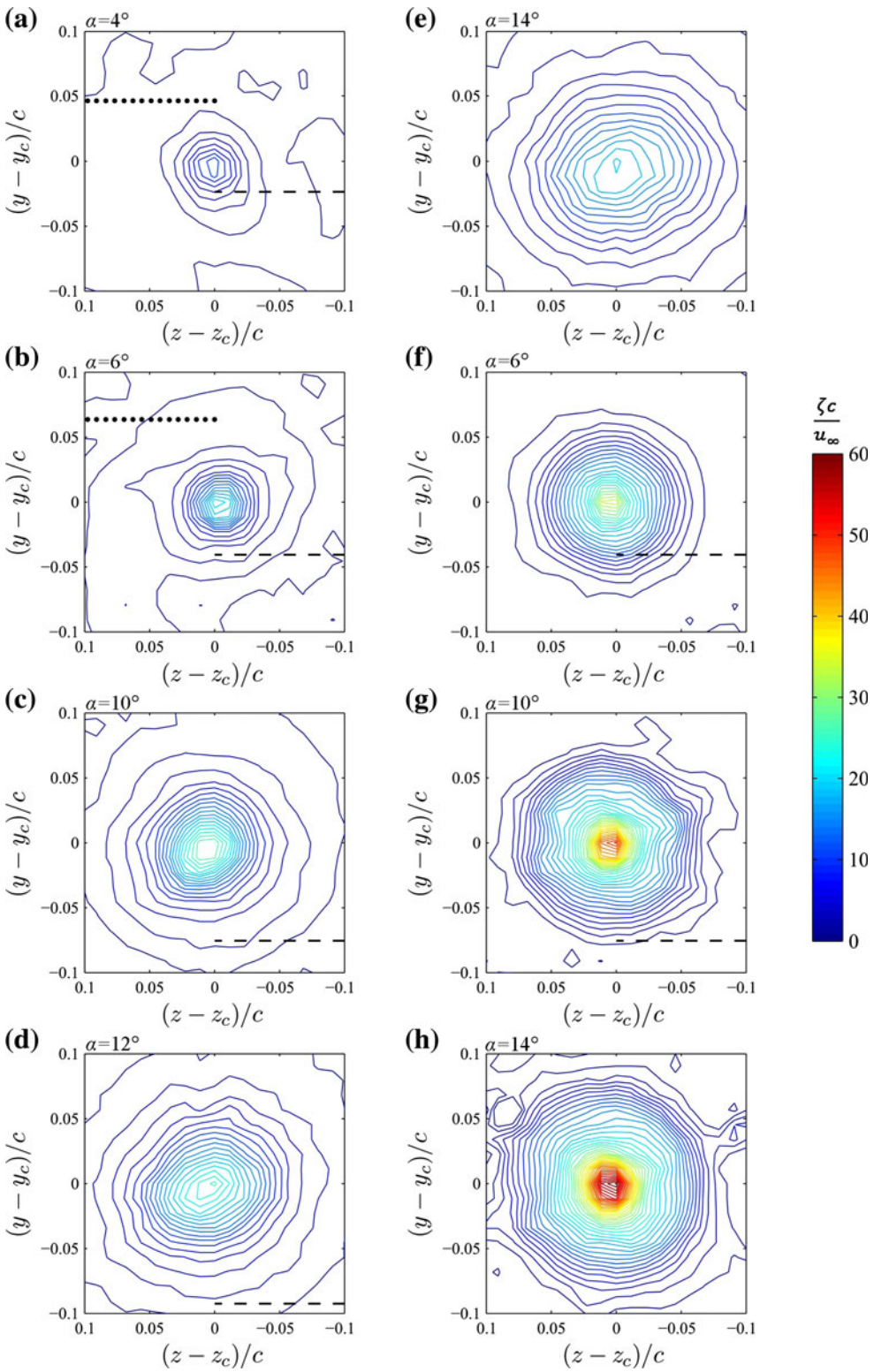

Fig. 3 Normalized iso-vorticity contours of the tip vortex at $x/c = 3$ for different α. **a–e** RHDW wing, **f–h** baseline wing. *Dashed line* and *dotted line* denote baseline-wing trailing edge and RHDW leading edge, respectively

fit constants were found to $a_1 = 1.815$, $a_2 = 1.961$, and $a_3 = 0.987$ for both wing models employed in the present study. The impact of the RHDW on the vortex trajectory is also summarized in Fig. 4e, f. The tip vortex generated behind the RHDW wing had a more significant inboard and upward movement compared to the baseline wing. The extent of the inboard and upward movement was, however, observed to lessen with increasing angle of attack. For the

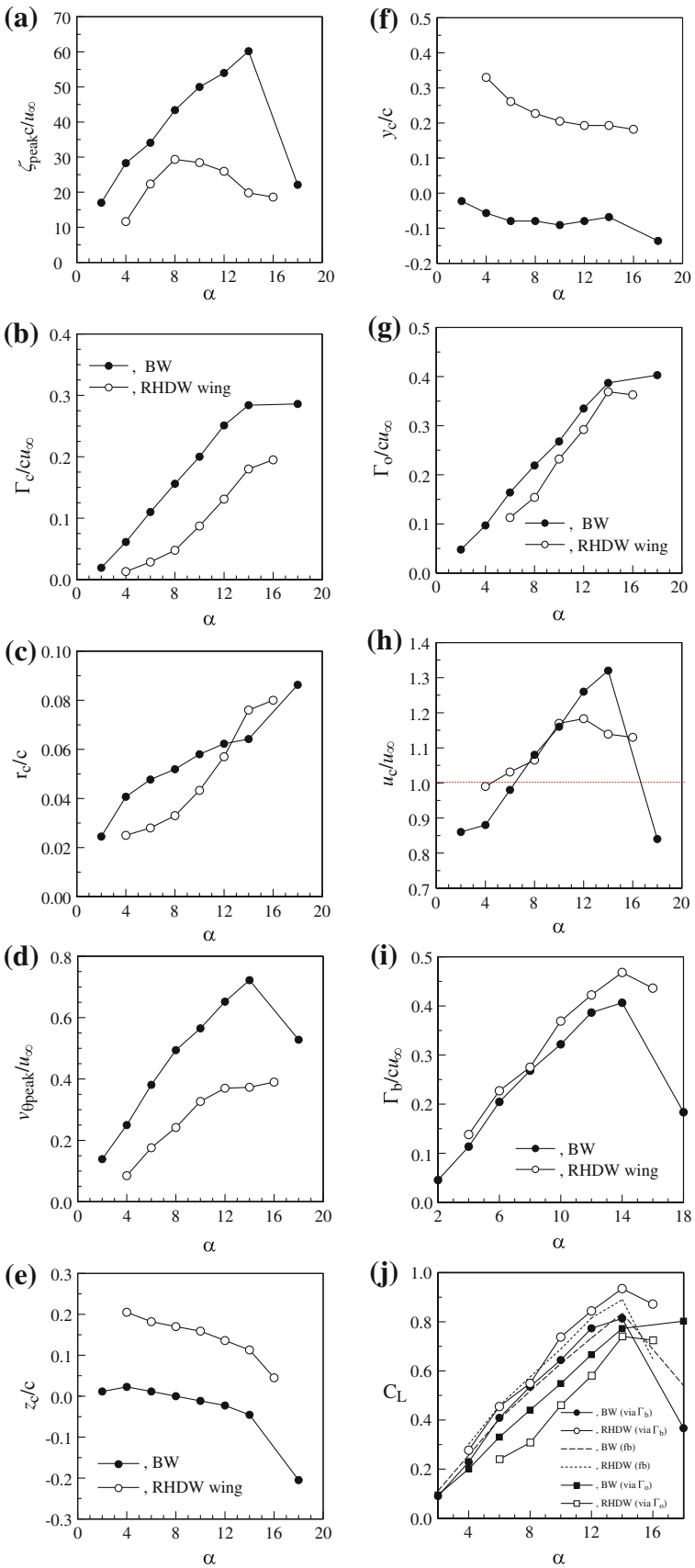

Fig. 4 **a–j** Impact of RHDW on vortex core flow characteristics at $x/c = 3$ for different α. fb denotes force balance

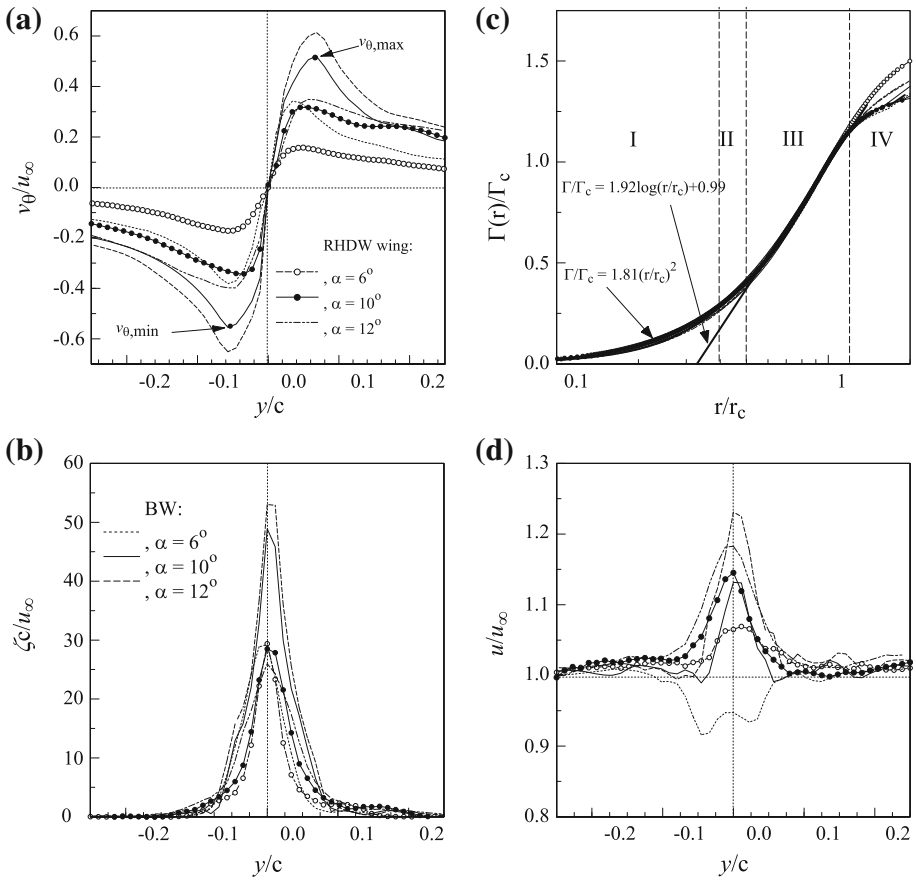

Fig. 5 Typical vortex flow distribution across vortex center at $x/c = 3$ for different α. *I* linear region, *II* buffer region; *III* logarithmic region; and *IV* wake region

baseline wing, the tip vortex, however, remained largely below the wing suction surface, as a result of a low-pressure wake region forming both behind and above the trailing edge of the baseline wing, which entrained the tip vortices and produced a downwash.

The corresponding change in the normalized total circulation Γ_o of the tip vortex at $x/c = 3$ for $\alpha = 2°$ to 16° is also summarized in Fig. 4g. The total circulation Γ_o was obtained based on the outer radius r_o (obtained by measuring the extent as the circulation $\Gamma(r_o)$ reached 95% of the total circulation). Γ_o was found to increase continuously with increasing α (for $\alpha \leq \alpha_{ss}$) for both wing models tested. The RHDW wing, however, had a lowered Γ_o compared to the baseline wing. For both wing models tested, the core strength had a constant fraction ($\approx$73%) of Γ_o, which is consistent with the theoretical value of $\Gamma_c/\Gamma_o = 0.715$ of Lamb's solution (1945). The spanwise circulation distribution $\Gamma(z)$ from the whole-wake measurement, up to 75% of the semi-span of the wing model, also allowed the extrapolation of the bound, or root, circulation Γ_b at the root. The spanwise determination was determined by computing the area integral of vorticity over the region of the scan outboard of z_i at each spanwise location z_i. Details of the $\Gamma(z)$ and Γ_b determinations are given in Birch and Lee (2004). The variation of Γ_b/cu_∞ with α is summarized in Fig. 4i. The RHDW wing had a higher Γ_b compared to the baseline wing, which is consistent with the C_L increment observed in Fig. 6a. For the baseline wing, the ratio of Γ_o/Γ_b was found to be about 0.8 (Fig. 4i, g), suggesting that at $x/c = 3$ and $Re = 2.45 \times 10^5$ about 80% of Γ_b was entrained into the tip vortex.

The force-balance measurements show that the RHDW wing had an increased C_L and lift-curve slope $C_{L\alpha}$ compared to the baseline wing at the same α (Fig. 6a). A 14% increment in C_L at $\alpha = 12°$, for instance, compared to the baseline wing was observed. The observed increase in C_L can be attributed to (1) the improved free end effects, which increased the suction pressure on the main wing in the tip region, (2) the increase in the wing area and the aspect ratio compared to the baseline wing, and (3) the RHDW-induced positive camber effects. The stall angle α_{ss} ($\approx$15°), however, remained largely unaffected due to the fact that the total surface area of the RHDW-equipped wing and subsequently the stalling mechanism were dominated by the NACA 0012 wing. Figure 6b reveals that, at the same angle of attack, the addition of the zero-setting 65° sweep RHDW produced a small increase in the total drag coefficient $C_D (= C_{D_p} + C_{D_i}$, where C_{D_p} is the profile drag

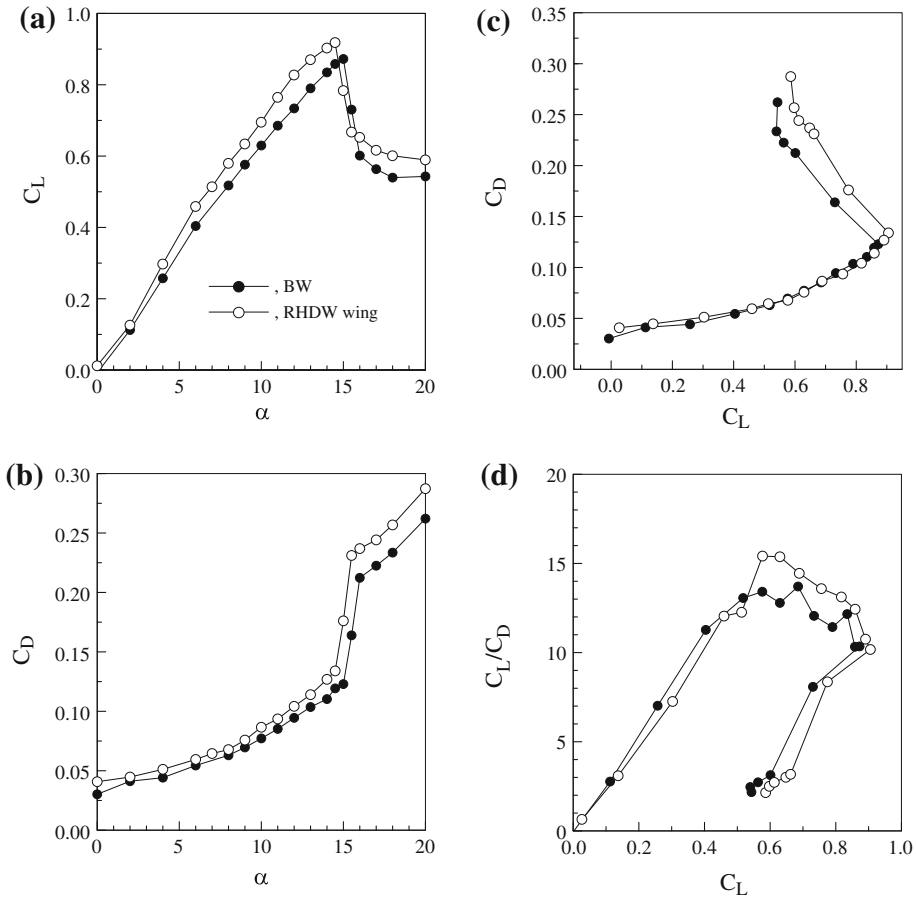

Fig. 6 Aerodynamic characteristics of RHDW-equipped wing and baseline wing

coefficient, which can also be obtained via wake momentum deficit, and C_{D_i} is the lift-induced drag coefficient) compared to the baseline wing. At the same lift condition, the change in C_D became insignificant (see Fig. 6c). In short, based on Fig. 6a–c, the RHDW configuration seems to possess an appealing aerodynamic performance (Fig. 6d), especially in the medium-to-high angles of attack range, at $Re = 2.45 \times 10^5$. The impact of the addition of RHDW on the values of C_{D_i} and C_{D_p} is discussed in Fig. 7.

The force-balance obtained lift coefficients were also compared with the C_L estimated based on Γ_o and Γ_b, respectively. Note that, for high Reynolds number or intuitively inviscid flows, the total circulation of the tip vortex of the baseline wing is also an indicative of the lift condition, and that the lift can be estimated by $L = 2\rho_\infty u_\infty \Gamma_o b' = \frac{1}{2}\rho_\infty u_\infty^2 C_L S$ relationship. b' is the effective span, which is twice the distance between the observable core of the trailing vortex and the wing center plane. Figure 4j reveals that the C_L estimated based on Γ_b is in good agreement with the force-balance data. For the baseline wing, the lift coefficient obtained from the total circulation of the tip vortex (i.e., via $C_L = 2b'\Gamma_o/u_\infty S$) was, however, found to be persistently lower than the force-balance data, due to the fact that the Γ_o only accounted for about 80% of Γ_b at this low Reynolds number. Special attention should also be given to the significantly lower C_L, estimated based on Γ_o, of the RHDW wing in comparison with the C_L obtained directly from the force balance. As explained in Fig. 2, in contrast to the tip vortex originated from the tip region of the rectangular baseline wing, the tip vortex generated behind the RHDW wing was originated from the leading edge of the RHDW. The C_L estimation based on Γ_o of the RHDW wing should therefore be perceived as a reference.

The lift-induced drag coefficient $C_{D_i}(= D_i/\frac{1}{2}\rho u_\infty^2 S$, where D_i is the lift-induced drag) was computed by using the Maskell induced drag model (1973), based on the vorticity inferred from the measured mean vw-velocity field. The cross-flow velocity vectors within the measurement plane were decomposed into a stream function $\psi(y, z)$ and a cross-flow velocity potential $\phi(y, z)$ with the imposed boundary conditions requiring both ψ and $\partial\phi/\partial n$ to be zero on the walls of the wind tunnel. The lift-induced drag was then obtained by Brune (1994) and Kusunose (1997, 1998)

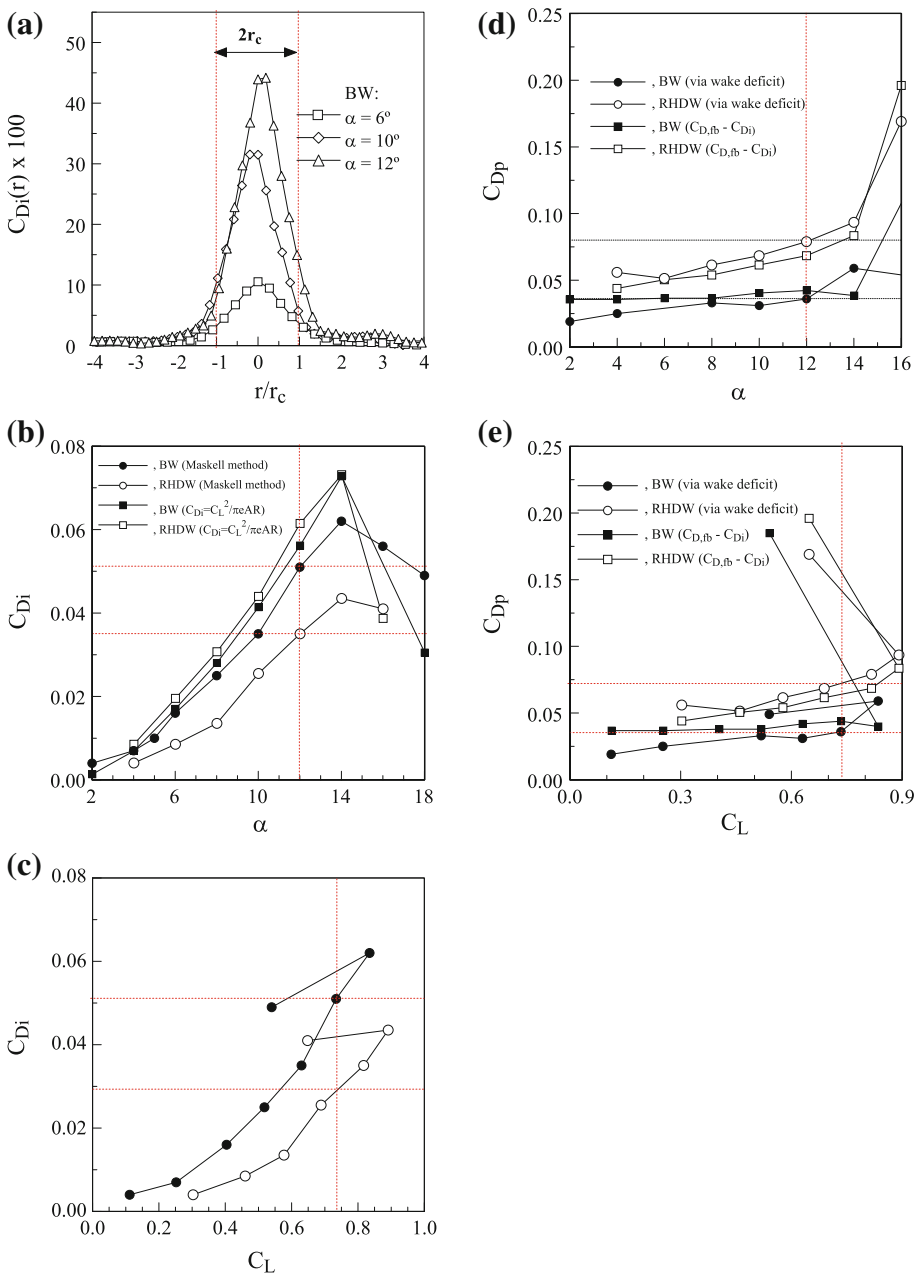

Fig. 7 Impact of RHDW on $C_{D_i}(r)$, C_{D_i}, and C_{D_p} at different α and C_L

$$D_i = \frac{1}{2}\rho_\infty \int_{S_\zeta}\int \psi\zeta \mathrm{d}y\mathrm{d}z - \frac{1}{2}\rho_\infty \int_{S_1}\int \phi\sigma \mathrm{d}y\mathrm{d}z - \frac{1}{2}\rho_\infty \iint \left(1 - M_\infty^2\right)(\Delta u)^2 \mathrm{d}y\mathrm{d}z \quad (1)$$

where $\zeta = \frac{\partial w}{\partial y} - \frac{\partial v}{\partial z}$ is the streamwise vorticity, and the surface S_ζ is the region within S_1 where the vorticity is nonzero. The third integral was introduced by Betz (1925) and is usually assumed to be negligible. The stream function $\psi(y, z)$ and velocity potential $\phi(y, z)$ are defined by the following relationships such that the vorticity and continuity equations are satisfied.

$$v = \frac{\partial \psi}{\partial z} + \frac{\partial \phi}{\partial y} \quad (2)$$

$$w = -\frac{\partial \psi}{\partial y} + \frac{\partial \phi}{\partial z} \quad (3)$$

The streamwise source term, which is small outside the viscous wake, can be defined as

$$\sigma = \frac{\partial v}{\partial y} + \frac{\partial w}{\partial z} = -\frac{\partial u}{\partial x} \quad (4)$$

To calculate the stream function and velocity, given a measurement grid of size $m \times n$, letting index i refer to the

row number and index j refer to the column number, we can re-express Eqs. 2 and 3 as

$$v_{j,i} = \frac{\psi_{j,i+1} - \psi_{j,i-1}}{2\Delta z} + \frac{\phi_{j+1,i} - \phi_{j-1,i}}{2\Delta y} \tag{5}$$

$$w_{j,i} = \frac{-\psi_{j+1,i} + \psi_{j-1,i}}{2\Delta y} + \frac{\phi_{j,i+1} - \phi_{j,i-1}}{2\Delta z}. \tag{6}$$

Since Δz and Δy, that is, the spanwise and transverse grid spacing, are identical, we can set $\Delta s^* = \Delta y = \Delta z$. If the grid spacing was not evenly distributed, the data can be redistributed using a linear interpolation scheme. Equations (4), (5), and (6) simplify to

$$2v_{j,i}\Delta s^* = \psi_{j,i+1} - \psi_{j,i-1} + \phi_{j+1,i} - \phi_{j-1,i} \tag{7}$$

$$2w_{j,i}\Delta s^* = -\psi_{j+1,i} + \psi_{j-1,i} + \phi_{j,i+1} - \phi_{j,i-1} \tag{8}$$

$$\sigma_{j,i} = \frac{w_{j+1,i} - w_{j-1,i}}{2\Delta s^*} + \frac{v_{j,i+1} - v_{j,i-1}}{2\Delta s^*}. \tag{9}$$

Assuming that the grid size is sufficiently large, we impose that the stream function and velocity potential are zero at the edge of the measurement grid:

$$\psi_{m,i} = \psi_{j,n} = \psi_{m,1} = \psi_{1,n} = 0 \tag{10}$$

$$\phi_{m,i} = \phi_{j,n} = \phi_{m,1} = \phi_{1,n} = 0 \tag{11}$$

From Eqs. 7 and 8, this leaves a $(m-2) \times (n-2)$ system of equations to be solved using matrix algebra

$$AX = B \tag{12}$$

Here, A is a square matrix of size $(m-2)(n-2) \times (m-2)(n-2)$ and B and X are $(m-2)(n-2)$ vectors

$$B = 2\Delta s^* \left[v_{2,2} v_{2,3} \cdots v_{2,n-1} v_{3,2} v_{3,3} \cdots v_{m-1,n-1} w_{2,2} w_{2,3} \cdots w_{2,n-1} w_{3,2} w_{3,3} \cdots w_{m-1,n-1} \right] \tag{13}$$

$$X = \left[\psi_{2,2} \psi_{2,3} \cdots \psi_{2,n-1} \psi_{3,2} \psi_{3,3} \cdots \psi_{m-1,n-1} \phi_{2,2} \phi_{2,3} \cdots \phi_{2,n-1} \phi_{3,2} \phi_{3,3} \cdots \phi_{m-1,n-1} \right] \tag{14}$$

Inverting A, we obtain the components of the stream function and velocity potential

$$X = A^{-1}B \tag{15}$$

Reinserting into Eq. 1 and applying a Riemann sum, the Maskell induced drag is calculated as

$$D_i \approx \frac{\rho_\infty}{2} \sum_{j=2}^{m-1} \sum_{i=2}^{n-1} \left(\psi_{j,i} \zeta_{j,i} - \phi_{j,i} \sigma_{j,i} \right) \Delta s^{*2}. \tag{16}$$

The radial distribution of the $C_{D_i}(r)$ is presented first in Fig. 7a. As can be seen, the magnitude of C_{D_i} was found to be dominated by the inner-flow region, covering up to $3r_c$, of the tip vortex for both baseline wing and RHDW wing. Details of the C_{D_i} computation scheme and its dependence on the measurement plane size, grid resolution, and the Reynolds number (for Re up to 1×10^6) can be found in the work of Gerontakos and Lee (2007). The impact of the RHDW on the lift-induced drag coefficient at different angles of attack and lift condition is summarized in Fig. 7b, c. The C_{D_i} was found to increase with α and C_L (for $\alpha < \alpha_{ss}$), regardless of the presence of RHDW. The addition of the zero-setting RHDW, however, produced a persistently lowered C_{D_i} compared to that of the baseline wing at the same α and C_L. A 33 and 42% reduction in C_{D_i} at $\alpha = 12°$ and $C_L = 0.734$, respectively, compared to the baseline wing was observed. Note that at this angle of attack, the value of C_{D_i} was also found to account for 34% of C_D compared to 42% of the baseline wing.

Also shown in Fig. 7b are the C_{D_i} estimated via

$$C_{D_i} = \frac{C_L^2}{\pi e \mathrm{AR}} \tag{17}$$

where e is called the span efficiency factor, or the Oswald's efficiency factor, which represents the divergence of the finite wing in question from the ideal elliptically loading (with $e = 1$). In this experiment, the e value was found according to Spedding and McArthur (2010) via

$$C_D = C_{D,0} + \frac{C_L^2}{\pi e \mathrm{AR}}. \tag{18}$$

A linear curve fit was imposed on plots of C_D against C_L^2. Care was taken to include only the linear portion of the curve, which was accomplished by carefully selecting a geometric angle of attack range to minimize the least squares deviation of the regressed curve fit. For the baseline case, the range selected was $\alpha = 0°$–$12°$, for which $e = 0.842$ of the baseline wing. The process was repeated for the RHDW wing, resulting in $e = 0.672$ for the range of $\alpha = 2°$–$11°$. Figure 7b shows that for the baseline wing the C_{D_i} estimated by Eq. 17 had a higher value than that computed by using the Maskell method (i.e., Eq. 1), which could be due to the low Reynolds number viscous flow effects encountered in the present experiments. Nevertheless, Eq. 17 can be used to obtain a quick estimation of the lift-induced drag coefficient. For the RHDW-equipped wing, the C_{D_i} was found to be greatly higher than that computed via Eq. 1 and was also larger than the baseline-wing value. It is our belief that the physical significance of using e to describe the effectiveness of the rectangular NACA 0012 wing with a tip-mounted RHDW could be questionable. Further investigations would be needed to support this argument. Also, in addition to the high sensitivity of the e value to AR, the AR of the RHDW-equipped wing might not be representative due to the planform of the RHDW, which is a half-delta configuration as opposed to a rectangular configuration. Thus, a small increase in span leads to a considerable increase in AR, while the planform area

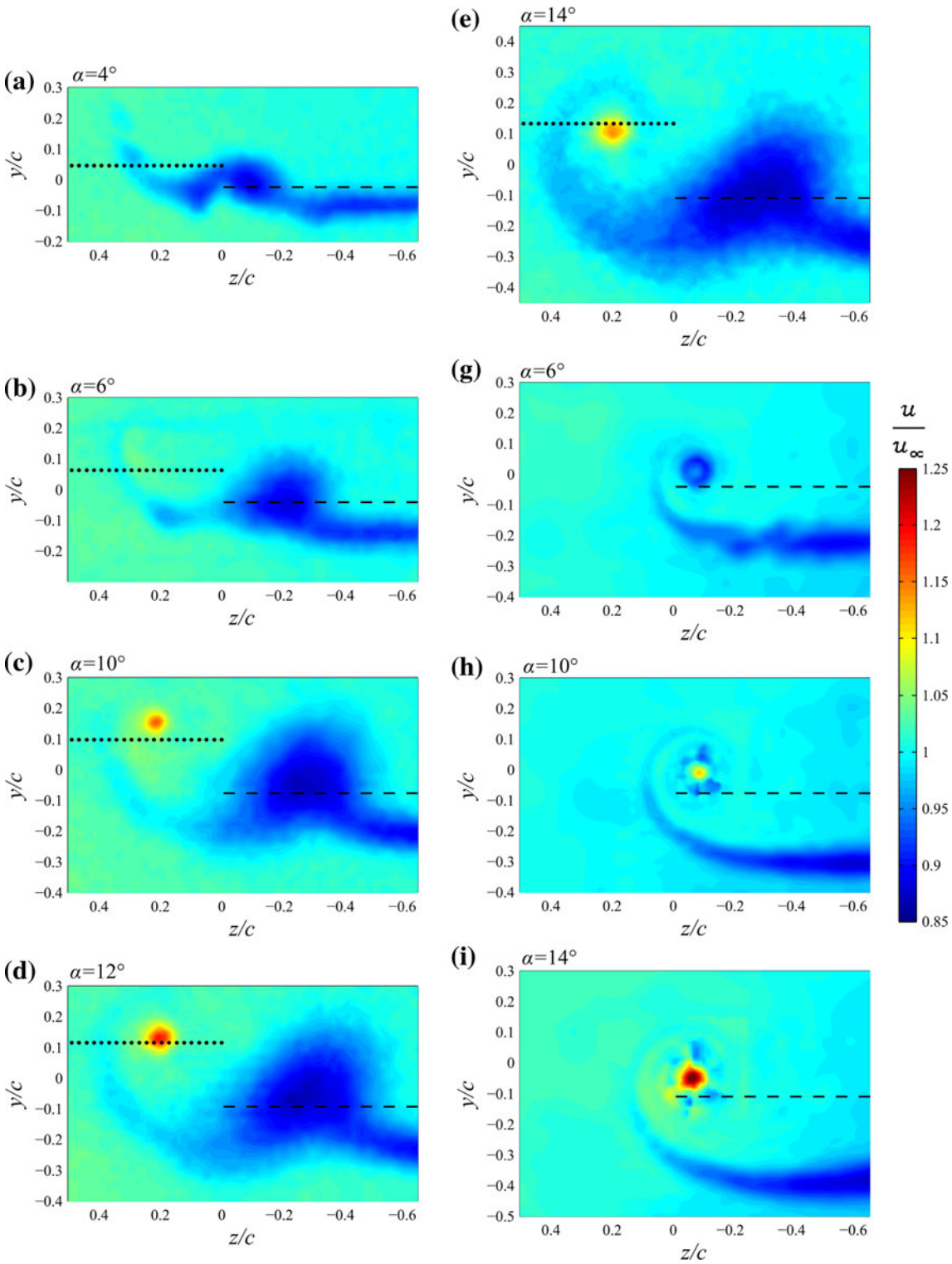

Fig. 8 Normalized mean iso-axial flow contours at $x/c = 3$ for different α. **a–e** RHDW wing, and **f–h** baseline wing

changes only slightly. The unrepresentatively high AR mathematically leads to a lower span efficiency, thus bringing into question the applicability of the span efficiency to this wing configuration.

The present whole-wake measurements further reveal that, in addition to the observed reduction in the strength and size and the lift-induced drag of the tip vortex, the presence of the RHDW also caused a drastic change in the

mean axial flow distribution (see Fig. 8a–e). The iso-u/u_∞ contours of the baseline wing at selected α are also presented in Fig. 8g, h for a direct comparison. Figure 8a–e show that, in addition to the axial vortex flow region associated with the tip vortex, a large wake-like separated flow region also exhibited downstream of the RHDW-equipped wing, rendering a unique "seahorse"-shaped iso-u/u_∞ flow pattern. This large separated wake was found to locate along and downstream of the juncture of the tip of the main wing and RHDW at smaller α and moved inward toward the main wing as α was increased. The higher the angle of attack the larger this separated wake region. This unexpected large separated wake was also found to produce an increased C_{D_p} compared to the baseline wing at the same α (Fig. 7d) and lift condition (Fig. 7e). Both C_{D_p} values, obtained from wake momentum deficit computation at $x/c = 3$ and by the subtraction of the force-balance C_D from C_{D_i} (i.e., $C_D - C_{D_i}$), are presented in these two figures. It is of interest to note that, for both wing configurations, the C_{D_p} was found to decrease noticeably with increasing x/c for x/c ≤ 1.5 and remains basically unchanged for $1.5 < x/c \leq 4$ in the present study. An 8–13% discrepancy was observed between these two sets of C_{D_p} values. This increase in C_{D_p} of the RHDW-equipped wing was, however, compensated by the reduction in C_{D_i} (Fig. 7b, c) and led to a minor variation in C_D compared to the baseline wing. Note that in order to better understand the physical mechanisms responsible for the observed "seahorse"-shaped axial flow distribution, the flow structure developed along the RHDW (i.e., for $x/c < 1$) was documented and is discussed in Fig. 9. Figure 8, together with Fig. 4h, further indicates that the u_c of the RHDW wing was always jet-like (for $\alpha \geq 4°$). For the baseline wing, the jet-like u_c was observed when α became larger than 8°; a wake-like u_c was observed for $\alpha < 8°$. The flow mechanisms responsible for the observed jet-like and wake-like core axial velocity of the baseline wing are given by Lee and Pereira (2010). Distributions of the mean axial velocity across the vortex center at selected α for $x/c = 3$ are also displayed in Fig. 5d.

3.2 Axial velocity and vorticity flowfields for $0 < x/c \leq 4$

The axial velocity and vorticity flowfields developed along the tip ($x/c < 1$) and in the near field ($1 < x/c \leq 4$) of both the RHDW wing and the baseline wing, positioned at $\alpha = 10°$, are presented three-dimensionally in Fig. 9a–c. For clarity, the enlarged views of the u/u_∞ and $\zeta c/u_\infty$ flowfields at $x/c = 0.4$ and 0.9 are also displayed in Fig. 10a–f. The void region in these figures, covering $x/c < 1$, denotes region not reachable by the sensor probe. The existence of the large wake-like flow region, which grew in size as it progressed downstream, can be clearly seen in Figs. 9a and 10a, b. This separated flow was created due to the breakdown of the spanwise leading-edge vortex filament as it was swept downstream toward the trailing apex point of the reverse full delta wing, as illustrated in Fig. 2c, f. Note that the smoke wire in Fig. 2c, f was purposely positioned to visualize the separated flow region developed on the upper surface of the reverse (full) delta wing. This vortex breakdown was triggered by high-pressure fluid flow escaped from the windward surface of the reverse delta wing, as well as by the instability of the spanwise vortex flow and its interaction with the wing upper surface boundary-layer flow. The downstream movement of this spanwise vortex breakdown or separated flow region was responsible for the "seahorse"-shaped iso-u/u_∞ contours discussed earlier in Fig. 8a–e. The variation of the normalized u_c is summarized in Fig. 11a, which shows that the u_c of the RHDW vortex was always jet-like for $0.3 < x/c \leq 4$. For the baseline wing, the u_c of the primary tip vortex was, however, wake-like for $x/c < 0.8$.

The evolution of the iso-$\zeta c/u_\infty$ flowfield of the RHDW vortex (for $x/c < 1$) and its subsequent development downstream (for $1 < x/c \leq 4$) is displayed in Figs. 9b and 10c, d. The formation and growth of the RHDW vortex was in consistency with the smoke-wire flow patterns presented in Fig. 2g, h. The RHDW vortex not only lied above the surface of the RHDW but also had a more rigorous rolling up process and a larger diameter (see Figs. 10c, d, 2d, e) in comparison with the vortex generated by the reverse (full) delta wing (as shown previously in Fig. 2a, b). The iso-$\zeta c/u_\infty$ contours both along the tip and in the near field of the baseline wing are also presented in Fig. 9c. In contrast to the presence of multiple secondary vortices and their entrainment into the primary tip vortex along the squared tip of the baseline wing (see, for example, Fig. 10e, f at $x/c = 0.4$ and 0.9), a more organized RHDW vortex with a higher ζ_{peak} value was observed for $x/c < 1$ (see also Fig. 11b). For $x/c > 1$, the peak vorticity, however, began to decrease continuously with increasing x/c and dropped below the baseline-wing value for $x/c > 1.5$. For the baseline wing, the ζ_{peak} of the primary tip vortex, however, increased along the wing tip, producing a local maximum at around $x/c = 0.95$, as a result of the entrainment of the secondary vortices by the primary tip vortex. The value of ζ_{peak} of the baseline wing then underwent a drastic drop at $x/c \approx 1$, as a consequence of the negative vorticity generated in the separated wake region, and remained basically unchanged for $1 < x/c \leq 4$. The variation in Γ_c with x/c, similar to that observed for ζ_{peak}, was also noticed (Fig. 11c). The baseline wing, however, exhibited a much higher Γ_c in comparison with the RHDW wing for $x/c > 1$. The variation of the

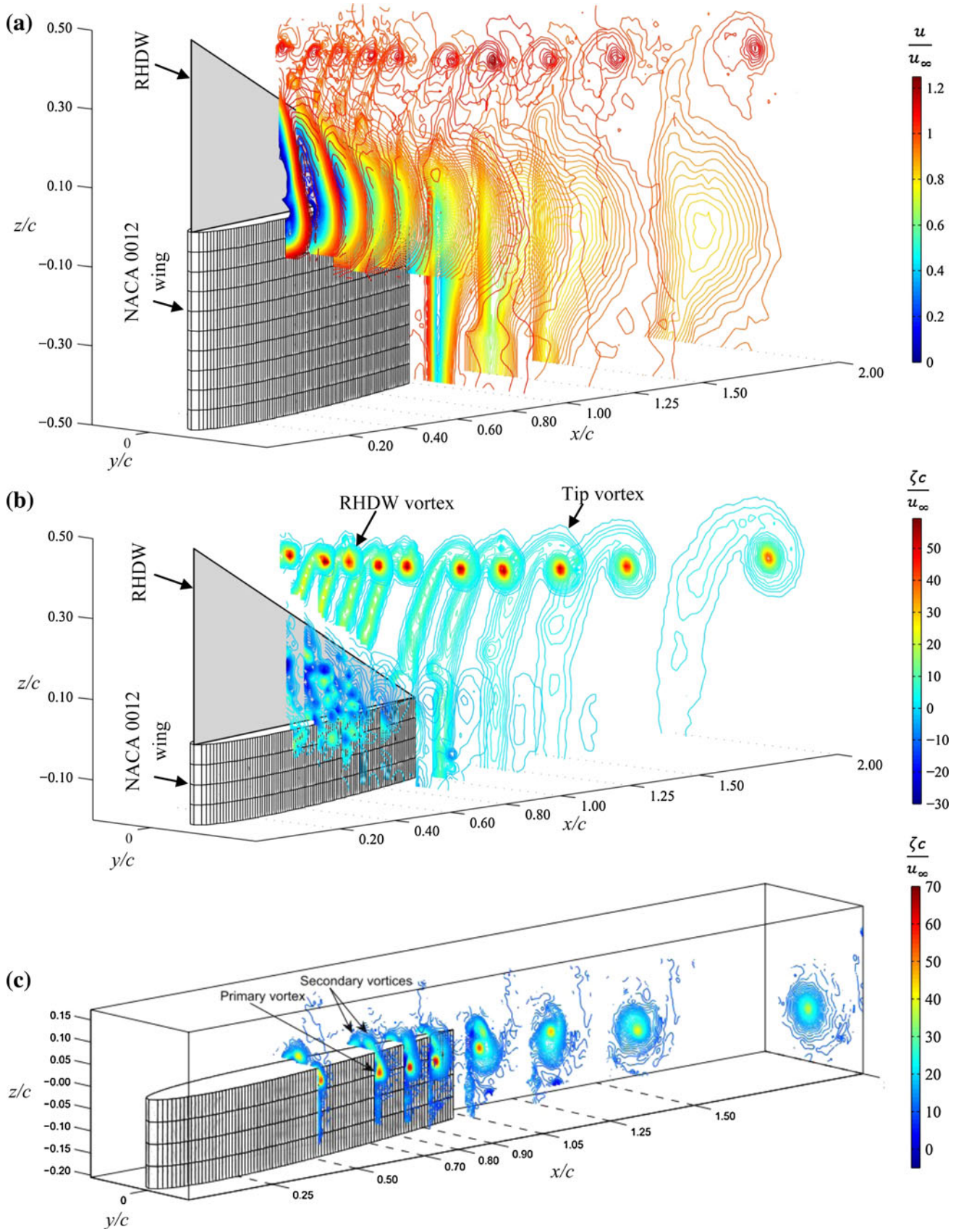

Fig. 9 3-D representation of iso-u/u_∞ and $\zeta c/u_\infty$ contours for $0 < x/c < 4$ at $\alpha = 10°$. **a**, **b** RHDW wing; and **c** baseline wing

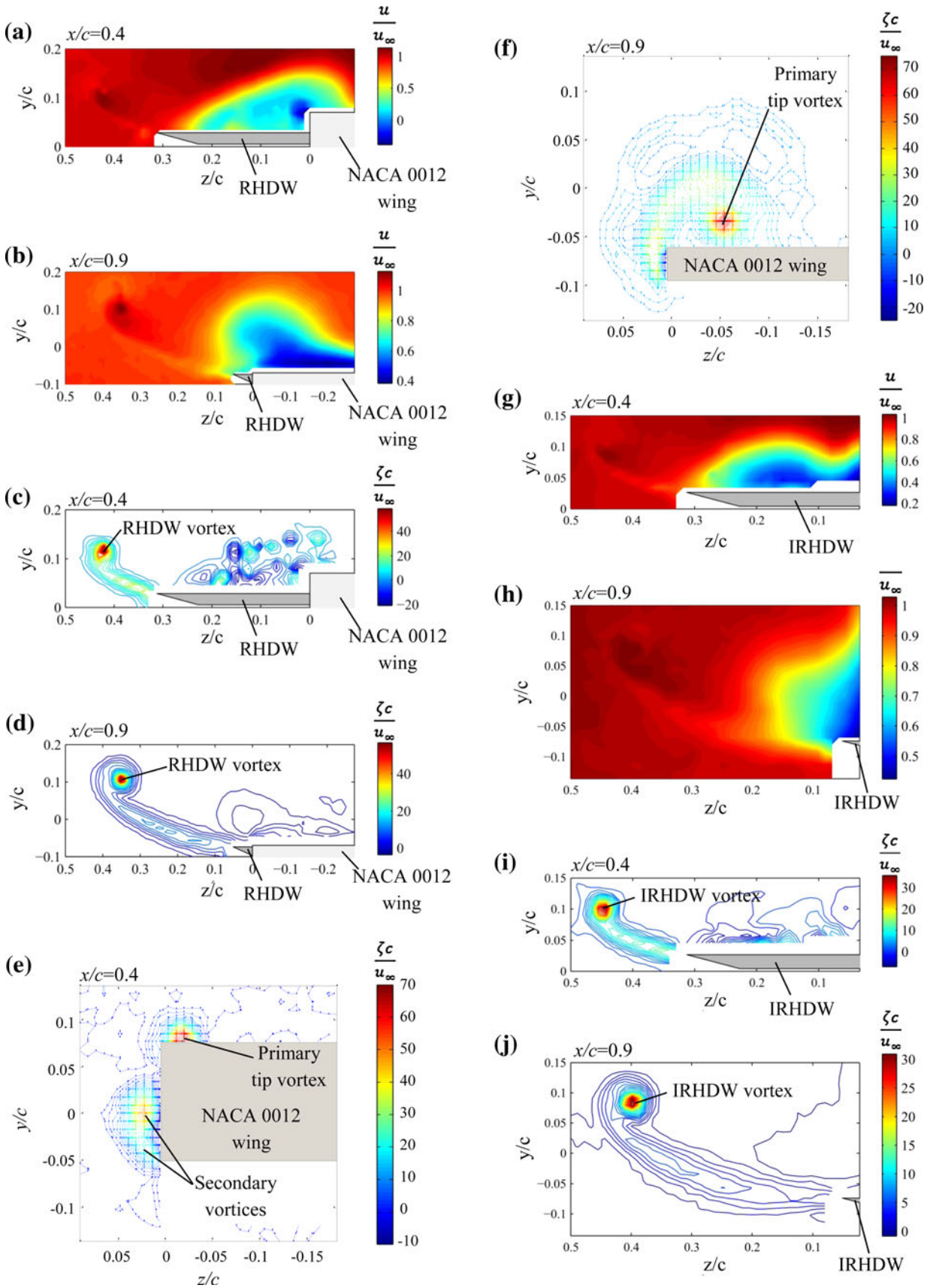

Fig. 10 Selected iso-u/u_∞ and $\zeta c/u_\infty$ contours at $x/c = 0.4$ and 0.9 for $\alpha = 10°$. **a–d** RHDW wing; **e**, **f** BW; and **g–j** IRHDW

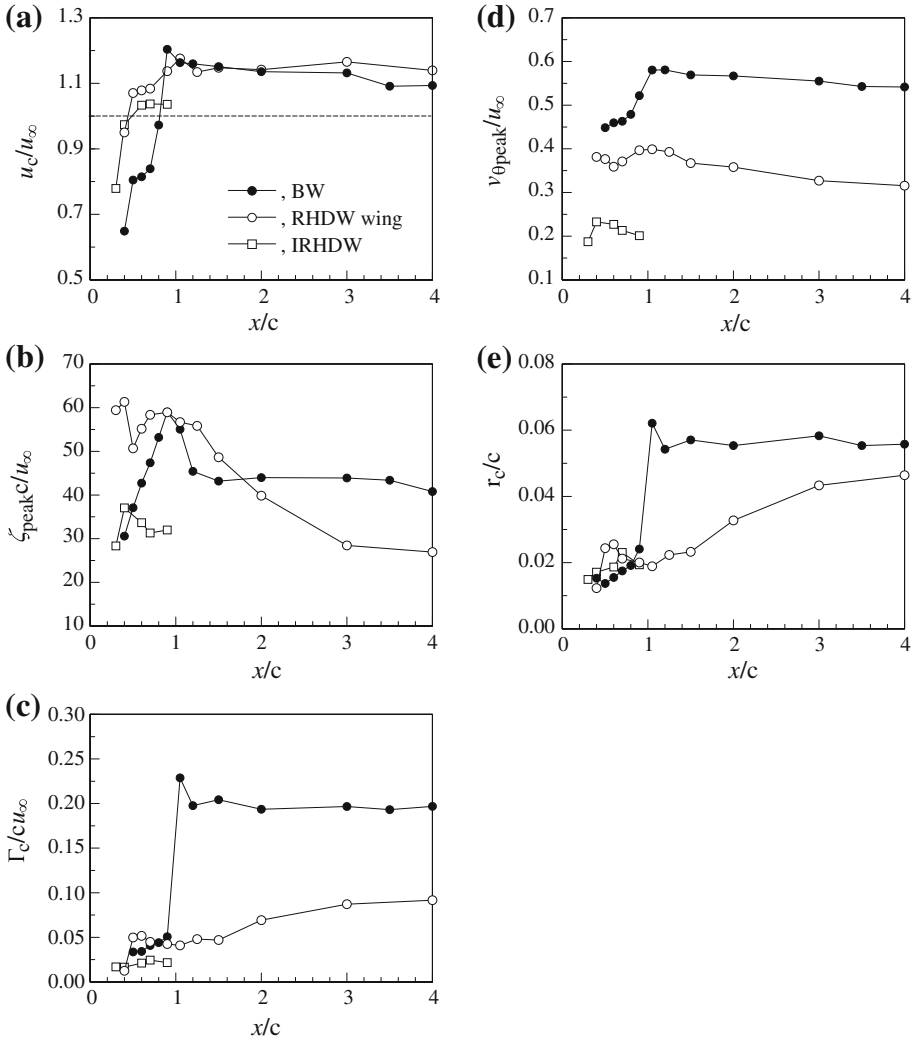

Fig. 11 Variation of normalized vortex core flow parameters with x/c at $\alpha = 10°$

circumferentially averaged $v_{\theta,peak}$ and r_c is also summarized in Fig. 11d, e. The RHDW wing produced a much lower $v_{\theta,peak}$ compared to the baseline wing, regardless of x/c (Fig. 11d). The core radius was, however, found to increase continuously with increasing x/c but remained below that of the baseline wing for $1 < x/c \leq 4$ (Fig. 11e).

Finally, the influence of the presence of the NACA 0012 wing on the formation and development of the RHDW vortex was also investigated at $\alpha = 10°$. To simulate the absence of the main wing, a 1.4-mm-thick sharp-edged disk (of a diameter of 40 cm) was inserted between the root of the RHDW and the squared tip of the rectangular NACA 0012 wing (see Fig. 1d). The iso-$\zeta c/u_\infty$ and u/u_∞ along the "isolated" RHDW or IRHDW at $x/c = 0.4$ and 0.9 were presented in Fig. 10g–j. The variation of the vortex flow characteristics of the IRHDW with x/c (for $x/c < 1$) is also summarized in Fig. 11. The large flow separation was persistently exhibited, due to the breakdown of the spanwise leading-edge vortex. The presence of the NACA 0012 wing gave rise to a pronounced difference in the velocity distribution at $y = 0$ and at the tip of the IRHDW. The presence of the NACA 0012 wing also produced an increased lower surface pressure of the RHDW, compared to that of the IRHDW, and subsequently led to the formation of the RHDW vortex with a higher u_c, ζ_{peak}, Γ_c, $v_{\infty,peak}$, and r_c in comparison with the IRHDW vortex (see Fig. 11a–e).

4 Conclusions

The effects of the RHDW, mounted at the tip of a rectangular NACA 0012 wing, on the vortex flow characteristics were explored experimentally at $Re = 2.45 \times 10^5$. The addition of the RHDW significantly modified the formation and characteristics of the tip vortex and led to a reduced lift-induced drag compared to the baseline wing. The RHDW wing-generated tip vortex had a lower vorticity level and a smaller peak tangential velocity and vortex size compared to the baseline wing. The presence of

the RHDW also created a large separated wake flow, which caused an increased profile drag compared to the baseline wing. The reduction in the lift-induced drag, however, outperformed the increase in the profile drag, resulting in a virtually unchanged total drag, at the same lift condition, compared to the baseline wing. This seemingly appealing change in the total drag, together with the RHDW-induced large lift increment, rendered an improved lift-to-drag performance, in the medium-to-high α range. Finally, the presence of the rectangular wing was found to have a rather significant influence on the axial flowfield of the tip vortex, generated behind the RHDW-equipped wing, but a large impact on its vorticity distribution.

Acknowledgments This work was supported by the Natural Science and Engineering Research Council (NSERC) of Canada.

References

Altaf A, Omar AA, Asrar W, Jamaluddin HBL (2011) Study of the reverse delta wing. J Aircraft 48(1):277–286

Aviation Week and Space Technology (2003) June, pp 15

Barlow JB, Rae WH, Pope A (1999) Low-speed wind tunnel testing. Wiley, New York, pp 367–390

Betz A (1925) A method for the direct determination of profile drag. ZFM 16:42–44

Birch D, Lee T (2004) The structure and induced drag of a tip vortex. J Aircraft 41(5):1138–1145

Breitsamter C (2008) Unsteady flow phenomena associated with leading-edge vortices. Prog Aerospace Sci 44:48–65

Brune GW (1994) Quantitative low-speed wake surveys. J Aircraft 31(2):249–255

Chow JS, Zilliac GG, Bradshaw P (1997) Mean and turbulence measurements in the near field of a wingtip vortex. AIAA J 35(10):1561–1567

Corsiglia VR, Schwind RG, Chigier NA (1973) Rapid scanning, three-dimensional hot-wire anemometer surveys of wing-tip vortices. J Aircraft 10:752–757

Elsayed OA, Asrar W, Omar AA (2008) Reverse delta wing trailing vortex characteristics by particle image velocimetry (PIV). In: 3rd international symposium on advanced fluid/solid science and technology in experimental mechanics, Tainan, 7–10 Dec

Francis MS, Kennedy DA (1979) Formation of a trailing vortex. J Aircraft 15:148–154

Gerontakos P, Lee T (2007) Lift-induced drag of a cambered wing for $Re < 1 \times 10^6$. Exp Fluids 42(3):363–369

Green SI, Acosta AJ (1991) Unsteady flow in trailing vortices. J Fluid Mech 227:107–134

Gursul I, Gordnier R, Visbal M (2005) Unsteady aerodynamics of non-slender delta wings. Prog Aerospace Sci 41(7):515–557

Hoffmann ER, Joubert PN (1963) Turbulent line vortices. J Fluid Mech 16:395–411

Kusunose K (1997) Development of a universal wake survey data analysis code. AIAA-97-2294

Kusunose K (1998) Drag reduction based on a wake-integral method. AIAA-98-2723

Lam H (1945) Hydrodynamics, 6th edn. Dover, New York, p 592

Lee S (1994) Reduction of blade-vortex interaction noise through porous leading edge. AIAA J 32(3):480–488

Lee L, Lee T (2006) Oscillating-wing tip vortex with short-span trailing-edge strip. J Aircraft 43(3):723–731

Lee T, Pereira J (2010) On the nature of wake- and jet-like axial tip-vortex flow. J Aircraft 47(6):1946–1954

Liu Z, Russell W, Sankar LN, Hassan AA (2001) A study of rotor tip vortex structure alternation techniques. J Aircraft 38(3):473–477

Maskell E (1973) Progress towards a method for the measurement of the components of the drag of a wing of finite span. RAE technical report 72232

McAlister KW, Takahashi RK (1991) NACA 0015 wing pressure and trailing vortex measurements. NASA TP-3151

Muller RHG (1990) Winglets on rotor blades in forward flight—A theoretical and experimental investigation. Vertica 14(1):31–46

Naik DA, Ostowari C (1990) Effects of nonplanar outboard of wing forms on a wing. J Aircraft 27(2):117–122

Nelson RC, Pelletier A (2003) The unsteady aerodynamics of slender wings and aircraft undergoing large amplitude maneuvers. Prog Aerospace Sci 39:185–248

Norris G (1998) Novel SST configuration revealed. Flight Int, 23 Dec 1998-5 Jan 1999

Phillips WRC (1981) The turbulent trailing vortex during roll-up. J Fluid Mech 105:451–467

Ramaprian B, Zheng Y (1997) Measurements in rollup region of the tip vortex from a rectangular wing. AIAA J 35(12):1837–1843

Robinson JJ (1996) A simulation-based study of the impact of aircraft wake turbulence weight categories on airport capacity. AGARD CP-584:1–15

Rossow V (1999) Lift-generated vortex wake of subsonic transport aircraft. Prog Aero Sci 35:507–660

Shekarriz A, Fu TC, Katz J, Huang T (1993) Near-field behavior of a tip vortex. AIAA J 31:112–118

Spalart PR (1998) Airplane trailing vortices. Ann Rev Fluid Mech 30:107–138

Spedding GR, McArthur J (2010) Span efficiencies of wings at low Reynolds numbers. J Aircraft 47(1):120–128

Spillman JJ (1978) The use of wing tip sails to reduce vortex drag. Aeronautical J 82:387–395

Tangler JL (1978) Experimental investigation of the subwing tip and its vortex structure. NASA CR-3058